

CCSNet: a deep learning modeling suite for CO₂ storage

Gege Wen^{a,*}, Catherine Hay^a, Sally M. Benson^a

^a*Energy Resources Engineering, Stanford University, 367 Panama St, Stanford, 94305, CA, USA*

Abstract

Numerical simulation is an essential tool for many applications involving subsurface flow and transport, yet often suffers from computational challenges due to the multi-physics nature, highly non-linear governing equations, inherent parameter uncertainties, and the need for high spatial resolutions to capture multi-scale heterogeneity. We developed CCSNet, a general-purpose deep-learning modeling suite that can act as an alternative to conventional numerical simulators for carbon capture and storage (CCS) problems where CO₂ is injected into saline aquifers in 2d-radial systems. CCSNet consists of a sequence of deep learning models producing all the outputs that a numerical simulator typically provides, including saturation distributions, pressure buildup, dry-out, fluid densities, mass balance, solubility trapping, and sweep efficiency. The results are 10³ to 10⁴ times faster than conventional numerical simulators. As an application of CCSNet illustrating the value of its high computational efficiency, we developed rigorous estimation techniques for the sweep efficiency and solubility trapping.

1. Introduction

Multiphase flow in porous media is important for many subsurface flow and transport problems such as hydrocarbon production [1] and carbon capture and storage (CCS) [2]. Numerical simulation is the primary tool used for predicting field-scale multiphase flow by solving spatially and temporally discretized mass and energy balance equations [3, 4, 5]. However, numerical simulation for multiphase flow problems is computationally expensive due to

*Corresponding author

Email address: gegewen@stanford.edu (Gege Wen)

the multiphysics problem nature [6], highly nonlinear governing partial differential equations (PDEs) [7], multiscale heterogeneity in the permeability field [8], and need for high spatial resolution of the grids [9, 10]. The inherent uncertainty in the subsurface geology necessitates probabilistic assessments and history matching [11], which often require prohibitively large numbers of simulation runs. To aid engineering decisions, ‘surrogate’ models with lower fidelity but greater computational efficiency are often developed for specific tasks [12, 13, 14, 15, 16].

Here we propose a deep learning approach for solving subsurface flow and transport problems with the fidelity of a traditional simulator and the speed of surrogate models or even faster. Unlike previous surrogate methods that are often developed on a ‘task’ basis [12, 13, 14, 15, 16, 17, 18, 19, 20], we demonstrate a deep learning tool, CCSNet, which can provide solutions to an entire class of multiphase flow problems, namely, CO₂ storage problems. CCS is a climate change mitigation technology that requires injection of supercritical CO₂ into saline aquifers for long term storage [21]. CCSNet can solve for nearly all realistic scenarios that entail injecting CO₂ into a 2d-radial system through a vertical injection well [22]. In such systems, the complex interplay between capillary, gravity, and viscous forces controls the migration of CO₂ [23, 24, 25, 10]. CO₂ migrates horizontally away from the injection well due to viscous forces while rising upwards due to to gravitational forces. Subsurface geological heterogeneity results in variations of permeability and capillary entry pressure [26, 8], which have a first-order effect on plume migration patterns, pressure buildup, trapping, and sweep efficiency [10]. Accurately modeling of these phenomena requires numerical simulations with high spatial and temporal resolutions [27, 9], making rigorous probabilistic assessments, optimization, and history matching for CO₂ storage especially computationally intensive using conventional numerical simulators.

Deep learning has recently shown a growing potential for applications to subsurface flow and transport problems [28, 18, 19, 17, 29, 20, 30, 31, 32, 33, 34]. Physics informed or physics constrained machine learning approaches encode governing PDEs in the loss function and solve the problem through automatic differentiation [28, 31, 32, 35]. To date, physics-informed machine learning models have not been successful in providing accurate approximations for hyperbolic PDEs that govern most multiphase flow problems [29]. Supervised learning approaches use data generated by numerical simulators to train deep learning models: these have shown encouraging results for specific uncertainty quantification or history matching tasks [19, 17, 36]. In fact,

supervised learning models can represent any complicated relationship given sufficient data and adequate training [37] and we develop CCSNet based on this principle. We demonstrate in this paper that deep learning tools have functionalities beyond merely used as task driven surrogate models. Instead, CCSNet provides solutions to a whole class of problems – in essence, for certain applications providing an alternative to conventional numerical simulation.

A major challenge for developing general-purpose tools for classes of problems is to design and create a training set that can fully represent the problem domain. Here we train CCSNet with a data set containing highly resolved and full-physics numerical simulation outputs that are representative of all realistic scenarios for 2d-radial CO₂ injection, including extensive ranges of reservoir conditions, fluid properties, geological attributes, rock properties, multiphase flow properties, and injection designs. Figure 1A shows the sequence of convolutional neural network (CNN) models in CCSNet that collaboratively provide predictions of salient outputs from conventional numerical simulators, namely, CO₂ gas saturation distribution, pressure buildups, the molar fractions of CO₂ and fluid densities for gas and liquid phases [38]. The full set of outputs allows us to evaluate how well the results satisfy the governing conservation equations without explicitly representing them in the loss function. CCSNet is nearly as accurate as numerical simulation for all realistic cases in the problem domain while being 10³ to 10⁴ times more computationally efficient. To demonstrate the value of CCSNet’s high computational efficiency, we used stochastic sampling of the problem domains to develop an estimation technique for sweep efficiency and solubility trapping, two of the important considerations when selecting sites for CCS projects.

2. Methodology

This section describes the governing equations, training data set generation, model architecture, data configuration, and training strategy of CCSNet.

2.1. Governing equations

For the CO₂ and water multiple-phase flow problem, the general form of mass accumulation for component $\kappa = CO_2$ or *water* is written as [38]:

$$\frac{\partial M^\kappa}{\partial t} = -\nabla \cdot \mathbf{F}^\kappa + q^\kappa, \quad (1)$$

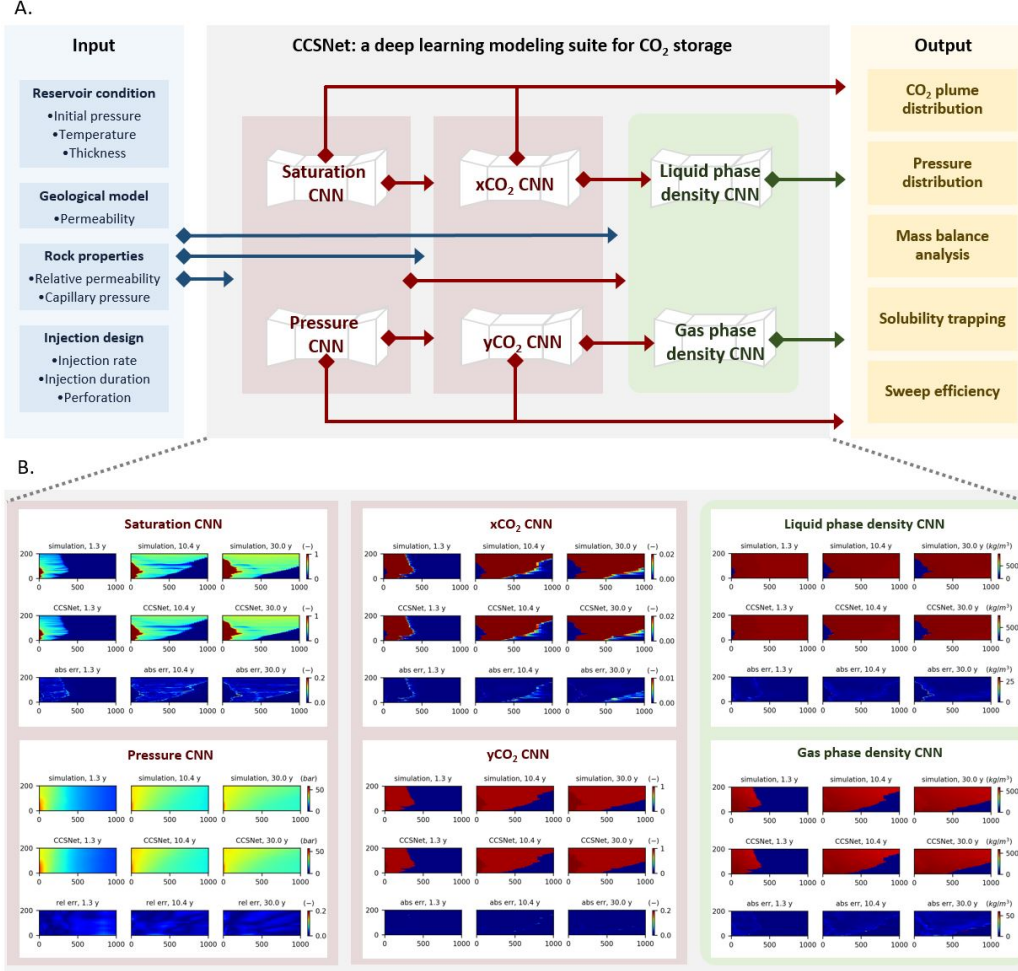


Figure 1: A. CCSNet’s inputs, prediction sequence, and outputs. The input section illustrates the four variable categories and specific variables in each categories. The prediction sequence section shows the 6 convolutional neural network (CNN) models. The output section shows the variables that CCSNet can produce. The arrows indicate the specific input and output for each model in the prediction sequence. B. Comparisons of the numerical simulation outputs, outputs predicted by CCSNet, and absolute/relative error at three arbitrary time snapshots for each model. The figures lie on the (r, z) coordinate. The r direction can extend to 100,000 m and the examples shown here are cropped.

For each component κ , the mass accumulation term M_κ is summed over phases p ,

$$M^\kappa = \phi \sum_p S_p \rho_p X_p^\kappa, \quad (2)$$

where ϕ is the porosity, S_p is the saturation of phase p , ρ_p is the density of phase p , and X_p^κ is the mass fraction of component κ presents in phase p . For each component κ , we also have the advective mass flux $\mathbf{F}^\kappa|_{adv}$ obtained by summing over phases p ,

$$\mathbf{F}^\kappa|_{adv} = \sum_p X_p^\kappa \mathbf{F}_p \quad (3)$$

where each individual phase flux \mathbf{F}_p is governed by Darcy's law:

$$\mathbf{F}_p = \rho_p \mathbf{u}_p = -k \frac{k_{r,p} \rho_p}{\mu_p} (\nabla P_p - \rho_p \mathbf{g}). \quad (4)$$

Here \mathbf{u}_p is the Darcy velocity of phase p , k is the absolute permeability, $k_{r,p}$ is the relative permeability of phase p , μ_p is the viscosity of phase p , and \mathbf{g} is the gravitational acceleration. The fluid pressure of phase p

$$P_p = P + P_c \quad (5)$$

is the sum of the reference phase (usually the gas phase) pressure P and the capillary pressure P_c . To simplify the problem setting, our simulation does not explicitly include molecular diffusion and hydrodynamic dispersion.

2.2. Training data set generation

We used the numerical simulator ECLIPSE (e300) to generate a large data set that is representative of most potential scenarios for CO₂ storage in deep geological formations. ECLIPSE is a state-of-the-art full physics numerical simulator that uses the finite difference system with upstream weighting and the adaptive IMplicit method for simulation [39]. The modeled volume is a radially symmetrical cylindrical volume that is 200m thick and 100,000m along the radius. The reservoir has no-flow boundaries on the top and bottom; the large radius mimics an infinite acting boundary on the radial direction. This geometry represents CO₂ injection into a regional-scale saline formation with a negligible dip, such as found in the Illinois Basin and parts of the North Sea and Gulf Coast. The modeled volume is isothermal and contains pure water prior to CO₂ injection. The vertical injection well is located at the center of the modeled volume, and the well radius is 0.1m. The injection well has no cross-flow, which means CO₂ can flow only from the well to the reservoir. The well has a single and continuous perforation and injects at a constant rate.

We used 96 uniform grid cells in the vertical direction and 200 gradually coarsened grid cells in the radial direction to represent the reservoir. This grid design is sufficiently refined to resolve the plumes in heterogeneous reservoirs while it remains computationally tractable for the purpose of training the deep learning models [10]. The numerical simulation runs for 30 years with 24 gradually coarsening time snapshots. Details of the temporal and spatial grid are discussed in Appendix A.

For each simulation case, we sample the inputs from the following four main categories.

2.2.1. Reservoir conditions

This category consists of formation thickness, initial pressure, and temperature, which are the most basic types of information available for any geological formation.

Existing machine learning-based methods for predicting subsurface flow problems usually suffer from fixed data dimensions, which significantly limits the models’ applicability. To account for the variable formation thicknesses, we assign extremely low permeability (10^{-7} mD) to layers in excess of the actual reservoir thickness. Using this method, CCSNet can handle formation thicknesses from 15m to 200m, which covers most of the known CO₂ storage projects operating today [40]. In future revisions, thicker reservoirs can also be included. The initial pressure and temperature in a formation depend on the depth and geothermal gradient. Formations that are too shallow are unsuitable for injection because CO₂ might not be in a super-critical state under reservoir condition; for formations that are too deep, drilling costs are prohibitively high for CO₂ storage [41]. Therefore, to generate realistic combinations of initial pressure and temperature, we first randomly sample the reservoir initial pressure from 100 to 300 bar, which corresponds approximately to formation depth from 1,000 to 3,000m. Subsequently, for the reservoir temperature, we sampled the geothermal gradient from 18 to 50 C°/km and created a wide range of temperature values from 35 to 170°C.

2.2.2. Geological model

The geological model describes the spatial distribution of permeability values. We train CCSNet with a data set containing various types of permeability maps. The permeability maps representing different depositional environments include a broad range of permeability values (10^{-3} mD to 10^2 D), a wide variety of horizontal and vertical correlations, and various permeability

distributions, such as Gaussian, non-Gaussian, bi-modal, multi-modal distribution, and uniform distributions (statistical characteristics summarized in Appendix B).

2.2.3. Rock properties

Commonly used rock property characteristic curves for CO₂ storage include relative permeability curves and capillary pressure curves. Both characteristic curves substantially impact the rate and direction of plume migration and are incorporated into CCSNet. To account for different relative permeability and capillary pressure curves, we sample the irreducible water saturation and van Genuchten function scaling factor according to references of rock types that can be used for CO₂ storage [42, 43]. The irreducible water saturation controls the relative permeability and capillary pressure characteristic curves. We used Corey’s curves to model relative permeability curves as a function of water phase saturation (S_w):

$$\begin{aligned} k_{r,w} &= S_w^{*n_w}, \\ k_{r,CO_2} &= k_{r,CO_2}(S_{wi})(1 - S_w^*)^2[1 - (S_w^*)^{n_{CO_2}}], \end{aligned} \quad (6)$$

where $k_{r,w}$ is the relative permeability of the water phase, k_{r,CO_2} is the relative permeability of the CO₂ phase, S_{wi} is irreducible water saturation, coefficient $n_w = 6$, coefficient $n_{CO_2} = 5$, coefficient $k_{r,CO_2}(S_{wi}) = 0.95$, and $S_l^* = (S_l - S_{wi})/(1 - S_{wi})$. To create different sets of relative permeability curves, we sampled S_{wi} from 0.1 to 0.3 in the training set.

The capillary pressure curves are modeled by the van Geneuchten function:

$$P_c = P_e[(S^*)^{-1/\lambda} - 1]^{1-\lambda}, \quad (7)$$

where P_c represents capillary pressure, P_e represents capillary entry pressure, and $S^* = (S_w - S_{wi})/(S_{ls} - S_{lr})$. Note that here we used an approximation of $S_{lr} = 0.999$ to represent the capillary entry pressure to avoid numerical errors in ECLIPSE. In the data set, we randomly sampled the scaling factor λ from 0.3 to 0.7 to create capillary pressure curves with different slopes. The capillary entry pressure is scaled according to the permeability in each grid cell by Leverett J-function:

$$P_e = \frac{\sqrt{k_{ref}/\phi_{ref}}}{\sqrt{k/\phi}} P_{ref}, \quad (8)$$

where $k_{ref} = 3.95 \times 10^{-15} \text{ m}^2$, $\phi_{ref} = 0.185$, and $P_{ref} = 7,500 \text{ Pa}$. For the van Genuchten curve, the S_{wi} is the same as in Corey’s curve.

2.2.4. Injection design

We created various combinations of injection rates, injection depths, and perforation thicknesses. In the training set, the maximum injection rate is 2 MT/year and the minimum injection rate is 0.02 MT/year. In addition to the injection rates, injection locations and perforation thicknesses also significantly influence the plume migration, especially in heterogeneous reservoirs. We created a wide range of injection strategies with the injection perforation interval thicknesses range from 15m to 200m; the top of the perforated interval is placed randomly within the depth interval of the injection well.

2.3. Model architectures

We designed a temporal-3d CNN model architecture for predicting the dynamic changes of CO₂ gas saturation, pressure buildup, molar fractions, and densities in each phases. The temporal-3d CNN consists of 3d convolutional kernels [44] that can extract information in both the temporal and spatial dimensions, which are adopted from state-of-the-art video classification and human action recognition models [45, 46]. Notably, we trained the temporal-3d CNN on data that has both non-uniform spatial and temporal dimension. Our results show that the temporal-3d CNN has excellent performance in non-uniform spatial-temporal systems, which significantly improved the models’ applicability. For the input/output regression mapping, we used an encoder-decoder structure that contains three major components: encoder, processor, and decoder (Figure 2).

The encoder maps the input 3d-volume to the input feature embedding. The processor learns the relationship between the input’s embedding and the output’s embedding using multiple 3d-ResConv blocks that we designed based on the well-known 2d-residual learning block [47]. The decoder projects the embedding of the output to the temporal-3d output space that represents the dynamic change of saturation, pressure, and dissolved phase molar fraction. Our work shows that the temporal-3d encoder-decoder architecture has performance superior to that of the U-Net based architectures [48] because, we hypothesize, the input and output exist in different spatial and temporal spaces.

The schematic in Figure 2 shows the network depth, and sizes of the Saturation CNN. For pressure, molar fractions, and densities in each phases, the depths and the sizes of the temporal-3d model architecture were optimized to provide accurate predictions each specific output. Parameters for each model are summarized in Appendix D, Appendix E, and Appendix F.

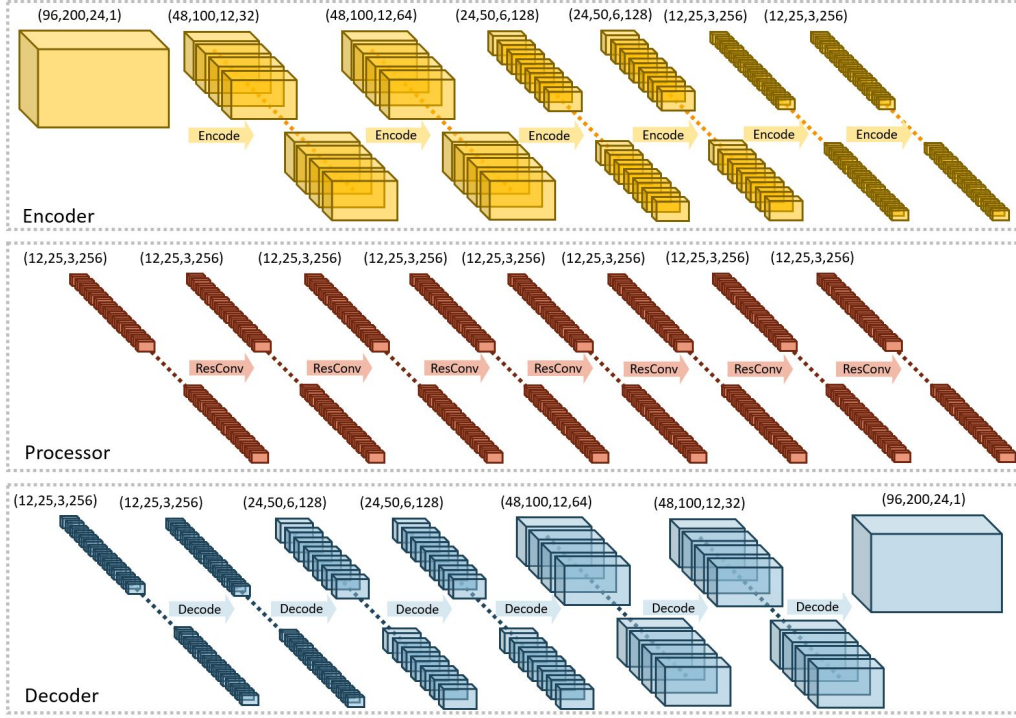


Figure 2: Model schematics of the Saturation CNN. The **Encode** operation consists of Conv3D/BN/ReLU; the **ResConv** operation consists of Conv3D/BN/Conv3D/BN/ReLU/Add; the **Decode** operation consists of UnSampling/Padding/Conv3D/BN/ReLU. The last dimension in the bracket denotes the number of channels.

2.4. Data configuration and augmentation

2.4.1. Outputs

Numerical simulation outputs at any arbitrary time step can be represented as 2d matrices in the dimension of 96×200 (r, z). The 2d matrices are stacked along the temporal dimension to construct the temporal-3d volume with the dimension of $96 \times 200 \times 24$ (r, z, t). The output data of gas saturation distribution, pressure buildup, molar fraction of CO_2 in the liquid phase ($x\text{CO}_2$) and gas phase ($y\text{CO}_2$), and densities in each phase are all configured in this manner.

To improve the training efficiency, we applied min-max normalization to the output values of pressure buildup and $x\text{CO}_2$. We also applied a data augmentation technique in addition the min-max normalization for the outputs of $y\text{CO}_2$ and densities in each phase. For these outputs, the magnitude

of the output values within the plume have a large difference comparing to the values outside the plume. For example, gas densities within a plume has magnitude of few hundreds (kg/m^3) with a small variation; gas density outside of a plume is always zero. Therefore, simply applying a min-max normalization to these outputs would suppress the details within the plume area. We used the data augmentation technique that casts the values outside the plume to be a constant slightly smaller than the minimum value within the plume. This technique allows us to maintained the details within the plume and produces highly accurate prediction for yCO_2 and densities in each phase.

2.4.2. Inputs

The inputs to the CNN models are designed to have the identical shape as the outputs. The high dimensional volume ($96 \times 200 \times 24$) provides room for incorporating all of the aforementioned input variables: reservoir conditions, geological attributes, rock properties and injection design. For each input, the permeability map and reservoir thickness are represented in a 96×200 matrix. The injection perforation location is represented by a binary matrix where only grid cells next to the perforation interval are marked by one. The variable of initial pressure, temperature, injection rate, irreducible water saturation, and van Genuchten scaling factor are scalar values which we broadcast into matrices in the dimension of 96×200 . These matrices are concatenated to construct the input volume in dimension of $96 \times 200 \times 24$. Notice that these input variables only populate 7 of the 24 slices available in the input volume. The idle slices are populated with permeability maps here and can be converted easily to directional permeability or porosity in the future.

The Saturation and Pressure CNNs both use this input volume as their training input. For the xCO_2 and yCO_2 CNNs, the prediction also requires the predicted gas saturation and pressure buildup in addition to the input volume. Therefore, we concatenated the gas saturation volumes, pressure buildup volumes, and the original input volumes to create a 4d training input with the dimension of $96 \times 200 \times 24 \times 3$. Similarly, for training the CNNs that predict the densities in each phase, we constructed a similar 4d input that consists of the formation temperature, pressure, and the molar fraction in the specific phase.

The training/validation data split is 10/1 with 19,000 training samples and 1,900 validation samples.

2.5. Training strategy

The loss function that we used is the Mean Square Error (MSE) loss:

$$L_{MSE} = \frac{1}{N} \sum_{i=1}^N \|\mathbf{y}_i - \hat{\mathbf{y}}_i\|_2^2,$$

where N is the number of training samples in a batch, \mathbf{y} is the true output in the data set, $\hat{\mathbf{y}}$ is the output predicted by the temporal-3d CNN model, described as $\hat{\mathbf{y}}_i = \mathbf{f}(\mathbf{x}_i, \theta)$, where θ is the model’s learnable parameters and \mathbf{x}_i is the input. During training, θ is updated based on the gradient to the loss function with respect to the θ (also referred to as back propagation in machine learning). We used the Adam optimizer [49] for the minimization of the loss function. The Glorot normal initializer [50] (also referred to as the Xavier normal initializer) was used to initialize the convolutional layers’ kernels in the CNNs. We applied L2 weight regularizers on the convolutional layers with a hyperparameter of 0.001 to reduce overfitting. The learning rate was initialized to be 10^{-4} and manually reduced to 10^{-7} throughout the training process. Our previous experiments show that the training efficiency of the CNNs is nearly insensitive to the choice of batch size [30]. The models were trained on NVIDIA v100 GPUs, and the training duration varied from a few days to a week.

3. Results

3.1. CO₂ gas saturation distribution

Using the temporal-3d CNN model illustrated in Figure 2, we trained the Saturation CNN to predict dynamic CO₂ gas saturation distributions as a function of space and time. Given information about the reservoir conditions, geological attributes, rock properties and injection patterns, the Saturation CNN generates predictions of dynamic CO₂ gas saturation distributions in ~ 0.05 s, which is more than 10^4 times faster than conventional numerical simulators (details on computing specifications in discussed in Section 4.1).

Figure 1B shows an example of the Saturation CNN’s prediction at several time snapshots in comparison with the numerically simulated output. This example demonstrates the multi-physics nature of the problem: the effects of viscous forces due to injection; the effects of gravity that lead to buoyancy induced flows; and spatially varying rock properties that locally counteract buoyancy. A dry-out zone also forms near the injection perforation, where

Table 1: Accuracy summary for model/output. All values were evaluated base on 1,000 randomly chosen samples. R^2 refers to the average scores in the training or validation set, μ refers to a mean, σ refers to a standard deviation, PAE refers to absolute errors within the plume; RAE refers to relative absolute errors for the whole field; PRE refers to relative errors within the plume.

Model / Output	Metric	Training	Validation	Unit
Saturation CNN	R^2	0.999	0.998	-
	μ_{PAE}	0.008	0.009	m^3/m^3
	σ_{PAE}	0.013	0.014	m^3/m^3
Pressure CNN	R^2	0.997	0.996	-
	μ_{RAE}	2.3	2.5	%
	σ_{RAE}	1.1	1.2	%
xCO ₂ CNN	R^2	0.998	0.998	-
	μ_{PAE}	1.58×10^{-4}	1.69×10^{-4}	mol/mol
	σ_{PAE}	6.60×10^{-5}	8.31×10^{-5}	mol/mol
yCO ₂ CNN	R^2	1.000	1.000	-
	μ_{PAE}	6.80×10^{-4}	8.09×10^{-4}	mol/mol
	σ_{PAE}	3.42×10^{-4}	4.41×10^{-4}	mol/mol
Liquid phase density CNN	R^2	1.000	1.000	-
	μ_{PRE}	0.05	0.06	%
	σ_{PRE}	0.06	0.06	%
Gas phase density CNN	R^2	1.000	1.000	-
	μ_{PRE}	0.01	-0.01	%
	σ_{PRE}	0.14	0.16	%
Mass balance	R^2_{liq}	0.999	0.999	-
	μ_{liq}	0.06	0.07	%
	σ_{liq}	0.68	1.07	%
	R^2_{gas}	1.000	1.000	-
	μ_{gas}	0.07	0.07	%
	σ_{gas}	0.76	0.93	%
	R^2_{total}	1.000	1.000	-
	μ_{total}	-0.09	0.08	%
	σ_{total}	0.74	0.85	%

the liquid-phase water vaporizes entirely into the gas phase. Although the dry-out is challenging for most numerical simulators due to the sharp gas saturation gradient, the Saturation CNN accurately predicts this in addition to the saturation variations caused by geological heterogeneity.

Based on a 1,000 randomly chosen examples, we show that the Saturation CNN is highly accurate (Table 1, Figure 3A). Similarly high R^2 values in the training and validation set demonstrate that the model has successfully learned the underlying relationship between the input parameters and

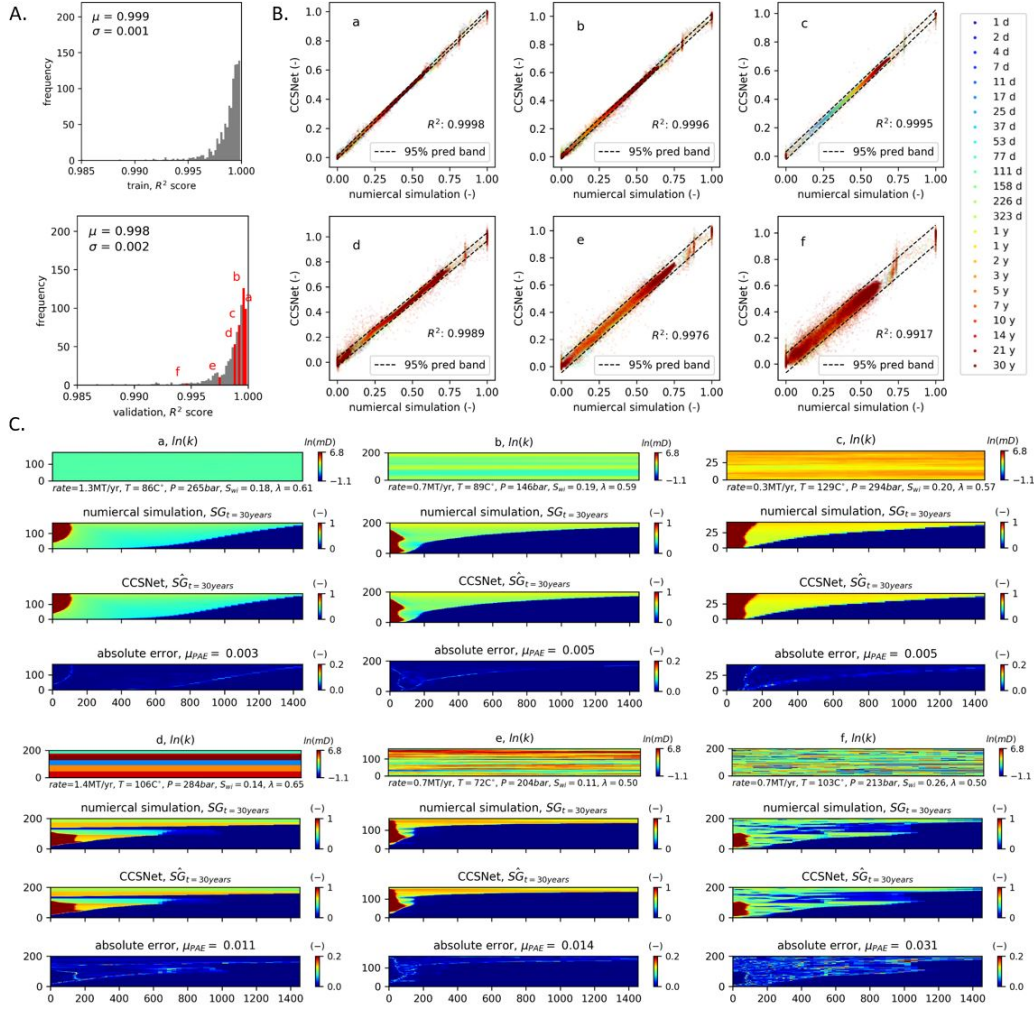


Figure 3: A. Histograms of Saturation CNN’s R^2 scores in the training and the validation set with the mean and standard deviation. On the validation set histogram, the red bars denote the R^2 score of the 6 examples in B and C. The alphabetical order corresponds to cases with R^2 scores at the 99, 95, 70, 30, 5, and 1 percentile. B. Gas saturation predicted by CCSNet vs. numerical simulation on each grid for the 6 examples. The colors of the points represent the injection duration. C. The permeability map, numerical simulation output, CCSNet predicted output, and absolute error for the 6 examples at 30 years. Inputs variables are summarized under each permeability map. The horizontal axes indicate the radial direction and the plume can extend out of the plot area. The mean absolute error within the plume (μ_{PAE}) is shown for each example. The reservoir thicknesses are marked on the vertical axes.

the corresponding saturation plume behavior instead of merely memorizing the training data. We use six examples in Figure 3B to demonstrate the prediction performance at different R^2 scores (ranked from high to low), in which we show that the Saturation CNN performs equally well throughout the prediction period and over the entire range of saturation values. Cases with smoother permeability maps are matched almost perfectly. Even for the most challenging example that is in the lowest 5% of the validation set, the predicted saturation distribution is in close agreement to the simulated output. The accuracy statistics provided in Table 1 indicate that the Saturation CNN provides predictions that are sufficiently accurate for predicting plume migration, sweep efficiency assessment, plume footprint prediction, and risk analysis.

3.2. Pressure buildup

We trained another temporal-3d CNN model, Pressure CNN (model parameters summarized in Appendix E), to predict the pressure buildup due to CO₂ injection. The Pressure CNN can be used independently from the Saturation CNN. Pressure buildup predictions take ~ 0.04 s. Figure 1B shows an example of the Pressure CNN’s output at various times, in which the CO₂ is injected in the lower half of the reservoir, creating a zone of high pressure buildup near the injection perforation.

Pressure buildups vary widely in the the reservoir and between cases, ranging from almost 400 bars near the injection well in over pressured reservoirs, to 0 bars near the reservoir boundary in highly permeable reservoirs. The Pressure CNN successfully accounts for the distinctly different pressure behaviors in different reservoirs and produces highly accurate predictions (Table 1, Figure 4A). The six examples in Figure 4C and D illustrate the excellent performance in predicting dynamic propagation of the pressure buildup in the reservoir throughout the injection period. Unlike saturation predictions where permeability heterogeneity dominates the performance, the Pressure CNN’s performance is correlated to the magnitude of pressure buildups, and poorest performance is for cases with the smallest pressure buildups (Figure 4B).

3.3. Mass balance analysis

Ability to accurately track the total mass balance and distribution of mass between phases is a critical measure of model performance and allows

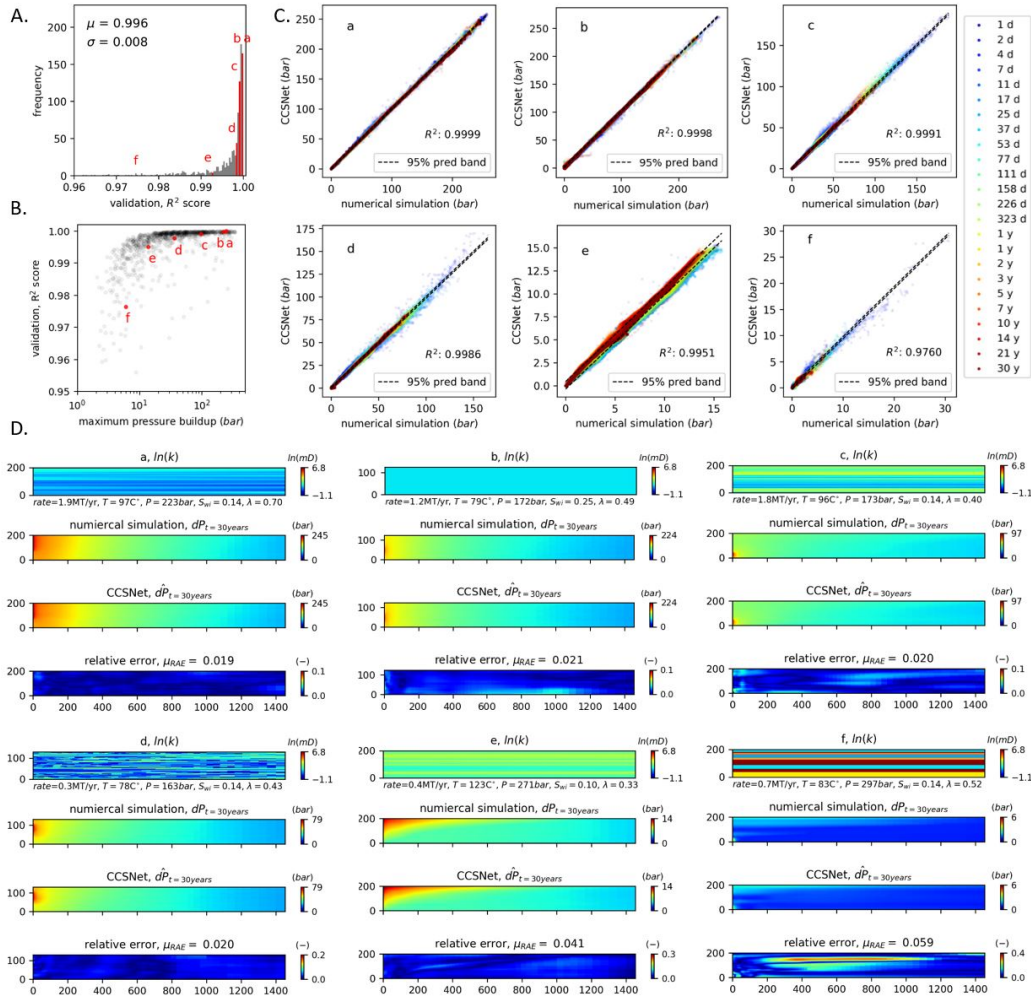


Figure 4: A. Histogram of Pressure CNN's R^2 scores in the validation set with the mean and standard deviation. The red bars mark the score of the 6 examples in B, C and D. The alphabetical order corresponds to cases with R^2 scores at the 99, 95, 70, 30, 5, and 1 percentile. B. Scatter plot of the R^2 scores vs. average pressure buildup. C. Pressure buildup predicted by CCSNet vs. numeral simulation on each grid for the 6 examples. The colors of the points represent the injection duration. D. The permeability map, numerical simulation output, CCSNet output, and relative error for the 6 examples at 30 years. Inputs for injection rate, temperature, initial pressure, irreducible water saturation, and capillary pressure scaling factor are summarized under the permeability map. The mean absolute relative error (μ_{RAE}) is shown for each case. The horizontal axes indicate the radial direction and the reservoir thicknesses, are marked on the vertical axes.

us to evaluate how well the deep learning outputs satisfy the governing conservation laws without explicitly representing the PDEs in the loss function. CCSNet uses six deep learning models to predict all the components needed to perform a mass balance (Figure 1A). The following equation describes the CO₂ mass balance in the reservoir at a given time step:

$$M = \sum_{i,n} V_n(\phi S \rho X)_{i,n} \quad (9)$$

where M is the total CO₂ mass, i denotes the phase (gas or liquid), n denotes the spatial grid, V is cell volume, ϕ is porosity, S is saturation, ρ is density, and X is the mass fraction of CO₂.

CCSNet generates each variable required in the mass balance analysis for the injected CO₂. The Saturation CNN provides $S_{i,n}$. Since the rock is compressible, the Pressure CNN is used together with the compressibility of the rock to predict $\phi_{i,n}$. Additionally, we developed and trained a model for predicting molar fractions of CO₂ in the liquid (xCO₂ CNN), a model for predicting molar fractions of CO₂ in the gas phase (yCO₂ CNN), as well as two models for predicting densities of the liquid and gas phases. Examples of each model’s output are shown in Figure 1B. Refer to Appendix C for details on the mass balance calculations.

3.3.1. xCO₂ CNN

Prediction of the molar fraction of dissolved CO₂ in the liquid phase (xCO₂) requires information about the gas saturation distribution, temperature, and pressure. CO₂ dissolves into the reservoir fluid wherever separate phase CO₂ is present. For the two-component system studied here, pressure and temperature control the solubility of CO₂. A small amount of dissolved CO₂ migrates in advance of the plume. No dissolved CO₂ appears in the dry-out zone near the injection well because the entire liquid phase is vaporized into the gas phase and transported away from the dry-out zone. Taking these factors into account, we use predicted outputs from the Pressure CNN and Saturation CNN in addition to the original input to train the xCO₂ CNN. Our experiments show that using this concatenated input significantly reduced over-fitting comparing to training with the original input.

The trained xCO₂ CNN performs very well (Table 1). Three examples in Figure 5B and C demonstrate the performance of the xCO₂ CNN. The prediction of xCO₂ CNN is more accurate in relatively homogeneous reservoirs where the dissolved phase xCO₂ stays close to the saturation plume

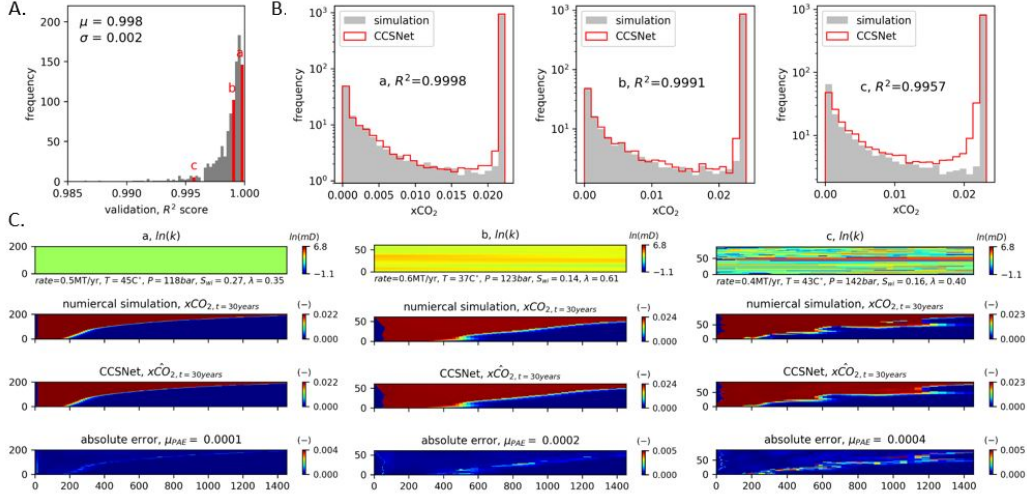


Figure 5: A. Histograms of $x\text{CO}_2$ CNN’s R^2 scores in the training and the validation set with mean and standard deviation. The red bars mark the score of the 6 examples in B and C. The alphabetical order corresponds to cases with R^2 scores at the 95, 50, and 5 percentile. B. Histogram comparisons between the numerical simulation’s output and CCSNet’s output within the plume for 3 examples. C. The permeability map, numerical simulation output, CCSNet output, and absolute error for 3 examples at 30 year. Inputs for injection rate, temperature, initial pressure, irreducible water saturation, and capillary pressure scaling factor are summarized under the permeability map. The mean absolute error within the plume (μ_{PAE}) is shown for each example. The horizontal axes indicate the radial direction, and the reservoir thicknesses are marked on the vertical axis.

front (Figure 5C.a). Heterogeneous cases such as Figure 5C.c are more challenging because dissolved CO_2 migrates in advance of the plume at various velocities.

3.3.2. $y\text{CO}_2$ CNN

The molar fraction of CO_2 in the gas phase depends on temperature and pressure. A small fraction of water vaporizes into the gas phase except in the dry-out zone, where the gas-phase contains nearly purely CO_2 . We trained the $y\text{CO}_2$ CNN to predict the molar fraction of CO_2 in the gas phase given the temperature, gas saturation predicted by Saturation CNN, and pressure predicted by Pressure CNN (model parameters summarized in Appendix F). The $y\text{CO}_2$ CNN provides excellent predictions for both the training and validation set (Table 1).

3.3.3. Fluid density CNNs

The fluid phase densities in the gas or liquid phase depends on the temperature, pressure, and molar fraction of CO_2 in that phase. Therefore, we trained two auxiliary CNNs to generate density predictions given temperature, pressure predicted by the Pressure CNN, and molar fraction predicted by the $x\text{CO}_2$ or $y\text{CO}_2$ CNN (model architecture in Appendix F). The trained fluid phase density CNNs are highly accurate (Table 1).

3.3.4. Error analysis

CCSNet generates accurate mass balances over the entire injection period (Table 1 and Figure 6). The largest errors occur during the first several days of injection. We hypothesize this is caused by a larger fraction of the CO_2 being in the liquid phase early in the injection process. The amount of CO_2 dissolved in the liquid phase is highly influenced by the artifacts of numerical dispersion at the leading edge of the plume. Therefore, at the beginning of the CO_2 injection, the training data are less systematic and challenging to learn. As injection goes on, a larger fraction of the CO_2 mass is in the gas phase, therefore the mass predictions becomes more accurate.

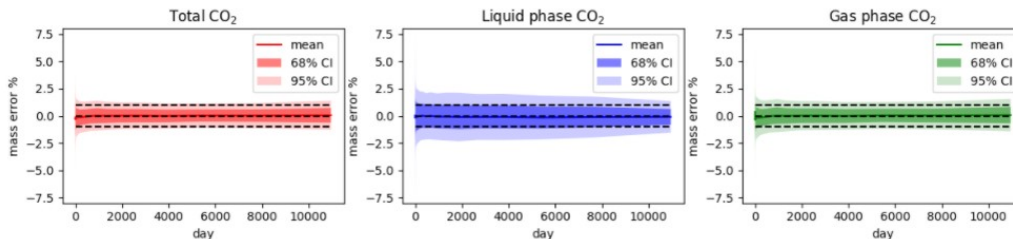


Figure 6: Mass balance error for the total, liquid phase, and gas phase CO_2 mass. The x-axes indicate the days of injection and the y-axes indicate percentage of the error. The black dotted dash lines are references for $\pm 1\%$. The light and dark shaded area are the 68% and 95% confidence intervals of the error.

Compared to physics informed machine learning approaches, supervised learning methods are criticized for the ‘lack of physics’ because the loss function does not explicitly describe the conservation laws and governing equations. However, our accurate mass balances together with the accurate distribution of CO_2 in both phases indicate that the supervised learning-based prediction sequence can satisfy the conservation laws and governing equations given sufficient data and training.

4. Discussion

4.1. Comparative computational efficiency

The average numerical simulation run time for 1,000 random cases using ECLIPSE (e300) is 10 minutes on an Intel[®] Xeon[®] Processor E5-2670 CPU. The numerical simulation run time for each simulation varies from 4 to over 100 minutes. Each simulation case utilizes a fully dedicated CPU, and the run time depends on the difficulty of the case.

To compare the computational efficiency, we used a NVIDIA v100 graphical processing units (GPUs) for CCSNet model inference. CCSNet’s prediction times have very small variances ($\sim 1\%$) compared to the conventional numerical simulator, and we computed computational efficiency based on the average of 1,000 random samples. The prediction time for the Saturation CNN and Pressure CNN are $\sim 0.05\text{s}$ and $\sim 0.04\text{s}$, respectively. Given the gas saturation and pressure buildup, the models for predicting the molar fraction of CO_2 in the liquid and gas phases each take $\sim 0.03\text{s}$. The gas and liquid phase fluid densities also require $\sim 0.03\text{s}$. Therefore, running the entire deep learning model sequence requires $\sim 0.22\text{s}$ to provide the full set of outputs that a numerical simulator can provide. The comparative speed-up between using CCSNet and ECLIPSE varies from 10^3 to 10^4 orders of magnitude depending on the information required by the particular analysis. For example, when predicting the sweep efficiency, we can run the Saturation CNN model by itself, which requires only $\sim 0.05\text{s}$. Calculating the solubility trapping requires outputs from the Saturation, Pressure, $x\text{CO}_2$, and liquid phase density CNNs, which adds up to $\sim 0.15\text{s}$. Average speed ups for relevant analyses are summarized in Table 2.

Table 2: Comparative computational efficiency of CCSNet. We used a NVIDIA v100 GPU for the model inference and the prediction time was calculated by taking the average of 1,000 random runs. The average ECLIPSE simulation run time in the training set (10 mins) was used for the comparison, where each simulation was carried out using an dedicated Intel[®] Xeon[®] Processor E5-2670 CPU.

Variable	Prediction time	Average speed up
Gas saturation distribution	0.05s	1.2×10^4
Pressure buildup	0.04s	1.5×10^4
Sweep efficiency	0.05s	1.2×10^4
Solubility trapping	0.15s	4.0×10^4
Mass balance	0.22s	2.7×10^3

4.2. Applications with fast prediction

Taking the advantage of the fast prediction speed of CCSNet, we develop a method for estimating sweep efficiency and solubility trapping using information that is often available for screening or comparing different CO₂ storage sites. In both cases, we stochastically sample the problem domains to develop a large ‘data set’ composed of 5,000 CCSNet runs to establish a relationship between the reservoir/operational properties and the sweep efficiency or solubility trapping. We sampled the homogeneous permeability from 1000mD to 5mD with a log-uniform distribution and the following variables with an uniform distribution: injection rate from 0.2 to 2 MT/yr, initial pressure from 80 to 160 bar, geothermal gradient from 22 to 28 °C/km, S_{wi} from 0.1 to 0.3, λ from 0.3 to 0.7, reservoir thickness from 15 to 200m, and perforation length from 15 m to the reservoir thickness. The sampled data set contains only those cases where the maximum pressure buildup is limited to 75% of the initial reservoir pressure. Here we use homogeneous reservoir characteristics since this is usually the only information available during site screening (e.g. in advance of detailed site-specific studies). By using CCSNet, the computational time for exhaustively sampling the domain is reduced from ~ 35 days to ~ 4 mins for sweep efficiency and ~ 12 mins for solubility trapping.

4.2.1. Sweep efficiency estimation

Sweep efficiency is a measure of how efficiently the storage space in a reservoir is used; the higher the sweep efficiency the better because higher sweep efficiency results in a smaller footprint of the CO₂ plume [51]. The footprint is the areal extent of the plume defined as πr_{max}^2 , where r_{max} refers to the largest distance away from the well that CO₂ has migrated. Sweep efficiency (E_{sweep}) is calculated as:

$$E_{sweep} = \frac{V_{gas}}{V_{r_{footprint}}} = \frac{\sum_n V_n \phi_n S_n}{\sum_{n \in footprint} V_n \phi_n}, \quad (10)$$

where V is the cell volume, ϕ is the porosity, S is the gas saturation, n denotes the spatial grid cell, and $n \in footprint$ denotes all grid cells within the the plume footprint. Using the gas saturation predicted by CCSNet, we find that E_{sweep} depends strongly on reservoir characteristics, ranges from as low as 0.01 to 0.2 over the sampled problem domain (Figure 7A). We

use CCSNet-generated E_{sweep} values as inputs into a non-linear multivariate regression algorithm (details in Appendix G) to develop an empirical relationship between E_{sweep} and reservoir/operational parameters.

$$E_{sweep} = \exp(0.05955 - 0.5258 \ln N_b - 1.390 \times 10^{-3} N_b + 0.2503 \ln(\frac{r_{inj}}{r_{ref}}) - 1.162 S_{wi} + \epsilon), N_b \in (10, 450) \quad (11)$$

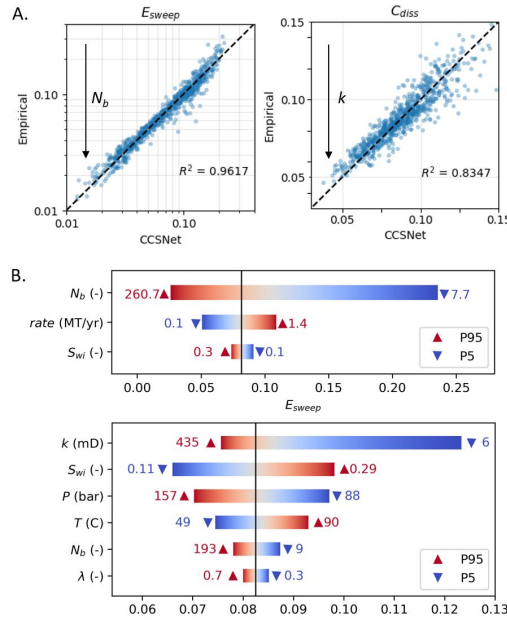


Figure 7: A. Comparisons of sweep efficiency and solubility trapping coefficient calculated using the empirical Equation 11 and 12 versus using CCSNet in the validation set. B. Coefficient sensitivity of each term in Equation 11 and 12. P5 and P95 represent the lowest 5th percentile and highest 95th percentile of the value for the term in the validation set.

Here N_b is the Bond number defined as $\Delta\rho g b_{res}/P_{cap}$ where b_{res} is the reservoir thickness and P_{cap} is the capillary entry pressure, S_{wi} is the irreducible water saturation, r is injection rate, and ϵ is the error term (reference values and details on each term summarized in Table G.7). As shown in Figure 7A, Eq. 11 is an excellent predictor of sweep efficiency over the range of Bond numbers from 10 to 450, as long as the injection rate is limited to comply with the 75% overpressure constraint. Previous studies have demonstrated that sweep efficiency and trapping are influenced by gravity number

and depositional environment [26, 52]. Here we show that for homogeneous reservoirs, the Bond number (N_b) has the largest influence on E_{sweep} ; reservoirs with lower Bond numbers have higher E_{sweep} (Figure 7B). E_{sweep} also increases with higher injection rates and lower S_{wi} values. Surprisingly, for the homogeneous reservoirs studied here, factors such as injection depth or injection interval had no significant influence on E_{sweep} . This would be expected to change for heterogeneous reservoirs.

4.2.2. Solubility trapping estimation

Solubility trapping occurs when CO₂ dissolves into the formation water and is beneficial for reducing the risk of CO₂ leakage [53, 54, 55]. Using a similar stochastic approach as described above, we developed an empirical expression for estimating solubility trapping (C_{diss}), where C_{diss} is the mass fraction of the injected CO₂ dissolved in the formation water:

$$C_{diss} = 0.0762 + 0.1804S_{wi} - 0.0030 \ln N_b + 0.2667 \frac{k_{ref}}{k} - 0.0149\lambda - 0.0964 \frac{P}{P_{ref}} + 0.0177 \frac{T}{T_{ref}} + \epsilon \quad (12)$$

where k is permeability, λ is the coefficient in van Genechuten capillary function, P is the initial pressure, and T is the temperature. Reference values and the error term are summarized in G.7. Solubility trapping is strongly influenced by a number of reservoir properties, with values ranging from 0.05 to nearly 0.15 (Figure 7A). In addition to the Bond number and S_{wi} , C_{diss} is also influenced by the formation permeability, initial pressure, temperature, and the coefficient in the capillary pressure function. Solubility trapping increases with lower permeability, higher reservoir temperature, lower pressure, and lower Bond number (Figure 7B). This result is counterintuitive, because the solubility of CO₂ in water increases with higher pressure and lower temperature. This analysis suggests C_{diss} is more strongly controlled by the density of the CO₂, which like C_{diss} , decreases with higher temperature and lower pressure. The lower the density of CO₂, the greater the plume volume, hence more contact area with the formation water and higher C_{diss} .

Note that the solubility trapping described here occurs during the injection phase of the CO₂ storage project. After injection stops, CO₂ will continue to dissolve as the result of convective mixing [56] and spreading [57], thus our estimates should be viewed as a lower bound. Additionally, we considered reservoirs with pure water; reservoirs with higher concentrations of

dissolved salts have lower solubility [58] and consequently smaller amounts of solubility trapping.

5. Conclusion and future work

We show that deep learning models such as CCSNet can provide an alternative to computationally intensive numerical simulators for routine tasks, such as predicting the injection performance of CO₂ storage projects. Important parameters such as the maximum extent of the CO₂ plume, saturation distributions, pressure buildup at the injection well and throughout the reservoir, sweep efficiency, and solubility trapping can be calculated accurately with high computational efficiency. While CCSNet includes many of the important parameters needed to realistically simulate the injection phase of a CO₂ storage projects, it is currently limited to systems well-represented by 2d-radial geometry and isotropic rock properties, and does not yet include post-injection processes such as residual gas trapping [59, 60] or mineral trapping [61, 62]. Nevertheless, the ability to train the model to perform the current tasks with such a high degree of accuracy, covering such a large domain of input parameters bodes well for increasing the capabilities of these models to include other features.

CCSNet has the flexibility to include additional input parameters and features when needed. As discussed in data configuration, the input volumes contain idle slices that can be used for other parameters. For example, the model currently uses isotropic permeability values. We can easily add anisotropy and porosity to the model by converting some slices into directional permeability and porosity. Similarly, relative permeability curves could be modified to include residual gas trapping [59].

The benefits of the high computational efficiency of CCSNet are evident from the new methods for estimating E_{sweep} and C_{diss} presented here. It is now possible to quickly provide reservoir-specific estimates of these parameters for screening prospective storage sites using data sets that are publicly available [63, 64, 65]. CCSNet can also be used once more site-specific data on geological heterogeneity is available to optimize injection depths and rates, make probabilistic predictions of plume footprint and pressure buildup, and for inverse modeling of monitoring data; all tasks required to support regulatory permit applications and compliance.

Web application

We developed a publicly accessible web application that hosts CCSNet. Users' can customize input variable combinations, including uploading their own permeability maps. The web application provides both independent and collaborative prediction to the models described above and produces outputs such as gas saturation, pressure buildup, solubility trapping, and sweep efficiency. Refer to <https://youtu.be/5bI1fjyo6Jk> for a video demonstration of this web application. The web application will be released to public upon the publication of this manuscript.

Code and data availability

The python code for CCSNet modeling suite and the data set used in training will be released upon the publication of this manuscript.

Acknowledgments

This work was supported by ExxonMobil through the Strategic Energy Alliance at Stanford University and the Stanford Center for Carbon Storage.

Appendix A. Grid resolution

The vertical grid dimension is $d_z = 200m/96 = 2.0833m$. The radial grid dimension is $d_r = 3.6m \times a^{i-1}$, where $a = 1.035012, i \in [1, \dots, 200]$. We used 24 time snapshots with gradually coarsening resolution to represent the total 30-year period where the time interval varies from days to years. Time step intervals $d_t = 1.421245^{i-1}$ days, where $i \in [1, \dots, 24]$. At early time steps, the CO₂ plume is located near the injection well where the spatial grid has high resolution. Capturing the variability between each time step requires high temporal resolution. Towards the end of the injection, because the plume migrates away from the injection well where the spatial grids are coarser, the coarse time resolutions are adequate. The temporal grid design also satisfies needs for operation that often requires finer time resolution monitoring at the beginning of injection.

Appendix B. Statistical characteristics of permeability maps

Table B.3: The permeability maps are generated using Stanford Geostatistical Modeling Software (SGeMS) [66]. SGeMS is an open-source computer package for geostatistical modeling according to user defined spatial variables. Here we defined the medium appearance, spatial correlation, mean, and contrast ratio (k_{high}/k_{low}) in each map to create a large variety of permeability maps. The permeability value for an individual cell can range from 10^{-3} mD to 10^2 D.

Medium	Parameter	Mean	Std	Max	Min	Unit
Gaussian	Field average	30.8	58.3	1053	0.3	mD
	Vertical correlation	7.3	3.6	12.5	2.1	m
	Horizontal correlation	2190	1432	6250	208	m
	Contrast ratio	4.01×10^4	2.19×10^5	3.00×10^6	1.01	-
von Karman [67]	Field average	39.9	54.4	867.9	1.8	mD
	Vertical correlation	7.2	3.5	12.5	2.1	m
	Horizontal correlation	2.15×10^4	1.40×10^4	6.23×10^4	208	m
	Contrast ratio	2.66×10^4	1.54×10^5	2.12×10^6	1.00	-
Discontinuous	Field average	80.8	260.2	5281	2.0	mD
	Vertical correlation	7.2	3.6	12.5	2.1	m
	Horizontal correlation	2176	1429	6250	208	m
	Contrast ratio	2.17×10^4	1.51×10^5	2.68×10^6	1.01	-
Layered	Field average	258.6	140.8	1022	5.4	mD
	Number of materials	10	5	20	2	-
	Contrast ratio	190.7	582.0	1.38×10^4	1.00	-
Homogeneous	Field permeability	327.7	478.1	1216	4.0	mD

Appendix C. Mass balance analysis

The discretized form of the mass accumulation term (Equation 2) at a given time step is written as:

$$M = \sum_{i,n} V_n(\phi S \rho X)_{i,n}, \quad (\text{C.1})$$

where n denotes the spatial grid and i denotes phase *gas* or *liquid*. CCSNet uses six models to collaboratively provide predictions to all the components. The Saturation CNN predicts the gas saturation which provides $S_{i,n}$; the fluid density CNNs provide $\rho_{i,n}$; the xCO₂ CNN and the yCO₂ CNN provide the molar fraction of CO₂ in each phase, which are thus used for calculating $X_{i,n}$. Since the reservoir rock is compressible, pore volume ϕ_n is a function of the pressure in each cell:

$$C_t = \frac{d\phi_n}{dP_n} \frac{1}{\phi_n}, \quad (\text{C.2})$$

where $C_t = 5 \times 10^{-4} \text{ bar}^{-1}$ represents the rock compressibility. The Pressure CNN predicts the pressure in each grid cell and the pore volume ϕ_n is adjusted as $\phi_n(P_n) = \phi_n(P_{n,ref})(1 + X + X^2/2)$, where $X = C_t(P_n - P_{n,ref})$ and $P_{n,ref} = 1.0132 \text{ bar}$.

Note that a neural network rarely predicts true zeros because the outputs are calculated empirically. Instead, zeros are represented by tiny numbers such as 10^{-6} . In the mass balance calculation, these tiny values in the predictions are amplified at grid cells that are far away from the injection well due to the large grid cell volume. Therefore, we applied cutoffs to the prediction of the Saturation and xCO₂ CNNs by casting gas saturation smaller than $1\text{e-}2$ and xCO₂ smaller than $8\text{e-}4$ to be zeros.

Appendix D. Saturation CNN architecture

Table D.4: Saturation CNN architecture. Conv3D denotes a 3D convolutional layer; c denotes the number of channels in the layer output; k denotes the kernel (also referred as filter) size; s denotes the size of the stride; BN denotes a batch normalization layer; ReLU denotes a rectified linear layer, Add denotes a addition with the identity; UnSampling denotes a unSampling layer that expands the matrix dimension using nearest neighbor method, and Padding denotes a padding layer using the reflection padding technique. In this model, the number of total parameters is 40,399,489 with 40,386,817 trainable parameters and 12,672 non-trainable parameters.

Part	Layer	Output Shape
Input		(96,200,24,1)
Encode 1	Conv3D(c32k3s2)/BN/ReLU	(48,100,12,32)
Encode 2	Conv3D(c64k3s1)/BN/ReLU	(48,100,12,64)
Encode 3	Conv3D(c128k3s2)/BN/ReLU	(24,50,6,128)
Encode 4	Conv3D(c128k3s1)/BN/ReLU	(24,50,6,128)
Encode 5	Conv3D(c256k3s2)/BN/ReLU	(12,25,3,256)
Encode 6	Conv3D(c256k3s1)/BN/ReLU	(12,25,3,256)
ResConv 1	Conv3D(c256k3s1)/BN/Conv3D(c256k3s1)/BN/ReLU/Add	(12,25,3,256)
ResConv 2	Conv3D(c256k3s1)/BN/Conv3D(c256k3s1)/BN/ReLU/Add	(12,25,3,256)
ResConv 3	Conv3D(c256k3s1)/BN/Conv3D(c256k3s1)/BN/ReLU/Add	(12,25,3,256)
ResConv 4	Conv3D(c256k3s1)/BN/Conv3D(c256k3s1)/BN/ReLU/Add	(12,25,3,256)
ResConv 5	Conv3D(c256k3s1)/BN/Conv3D(c256k3s1)/BN/ReLU/Add	(12,25,3,256)
ResConv 6	Conv3D(c256k3s1)/BN/Conv3D(c256k3s1)/BN/ReLU/Add	(12,25,3,256)
ResConv 7	Conv3D(c256k3s1)/BN/Conv3D(c256k3s1)/BN/ReLU/Add	(12,25,3,256)
ResConv 8	Conv3D(c256k3s1)/BN/Conv3D(c256k3s1)/BN/ReLU/Add	(12,25,3,256)
Decode 6	UnSampling/Padding/Conv3D(c256k3s1)/BN/Relu	(12,25,3,256)
Decode 5	UnSampling/Padding/Conv3D(c256k3s2)/BN/Relu	(24,50,6,256)
Decode 4	UnSampling/Padding/Conv3D(c128k3s1)/BN/Relu	(24,50,6,128)
Decode 3	UnSampling/Padding/Conv3D(c128k3s2)/BN/Relu	(48,100,12,128)
Decode 2	UnSampling/Padding/Conv3D(c64k3s1)/BN/Relu	(48,100,12,64)
Decode 1	UnSampling/Padding/Conv3D(c32k3s2)/BN/Relu	(96,200,24,32)
Output	Conv3D(c1k3s1)	(96,200,24,1)

Appendix E. Pressure CNN architecture

Table E.5: Pressure CNN architecture. Conv3D denotes a 3D convolutional layer; c denotes the number of channels in the layer output; k denotes the kernel (also referred as filter) size; s denotes the size of the stride; BN denotes a batch normalization layer; ReLu denotes a rectified linear layer, Add denotes a addition with the identity; UnSampling denotes a UnSampling layer that expands the matrix dimension using nearest neighbor method, and Padding denotes a padding layer using the reflection padding technique. Total params: 33,316,481, trainable params: 33,305,857, non-trainable params: 10,624.

Part	Layer	Output Shape
Input		(96,200,24,1)
Encode 1	Conv3D(c32k3s2)/BN/ReLu	(48,100,12,32)
Encode 2	Conv3D(c64k3s1)/BN/ReLu	(48,100,12,64)
Encode 3	Conv3D(c128k3s2)/BN/ReLu	(24,50,6,128)
Encode 4	Conv3D(c128k3s1)/BN/ReLu	(24,50,6,128)
Encode 5	Conv3D(c256k3s2)/BN/ReLu	(12,25,3,256)
Encode 6	Conv3D(c256k3s1)/BN/ReLu	(12,25,3,256)
ResConv 1	Conv3D(c256k3s1)/BN/Conv3D(c256k3s1)/BN/ReLu/Add	(12,25,3,256)
ResConv 2	Conv3D(c256k3s1)/BN/Conv3D(c256k3s1)/BN/ReLu/Add	(12,25,3,256)
ResConv 3	Conv3D(c256k3s1)/BN/Conv3D(c256k3s1)/BN/ReLu/Add	(12,25,3,256)
ResConv 4	Conv3D(c256k3s1)/BN/Conv3D(c256k3s1)/BN/ReLu/Add	(12,25,3,256)
ResConv 5	Conv3D(c256k3s1)/BN/Conv3D(c256k3s1)/BN/ReLu/Add	(12,25,3,256)
ResConv 6	Conv3D(c256k3s1)/BN/Conv3D(c256k3s1)/BN/ReLu/Add	(12,25,3,256)
Decode 6	UnSampling/Padding/Conv3D(c256k3s1)/BN/Relu	(12,25,3,256)
Decode 5	UnSampling/Padding/Conv3D(c256k3s2)/BN/Relu	(24,50,6,256)
Decode 4	UnSampling/Padding/Conv3D(c128k3s1)/BN/Relu	(24,50,6,128)
Decode 3	UnSampling/Padding/Conv3D(c128k3s2)/BN/Relu	(48,100,12,128)
Decode 2	UnSampling/Padding/Conv3D(c64k3s1)/BN/Relu	(48,100,12,64)
Decode 1	UnSampling/Padding/Conv3D(c32k3s2)/BN/Relu	(96,200,24,32)
Output	Conv3D(c1k3s1)	(96,200,24,1)

Appendix F. $x\text{CO}_2$, $y\text{CO}_2$, and fluid densities CNN architecture

Table F.6: $x\text{CO}_2$, $y\text{CO}_2$, gas phase density, and liquid phase density CNN architecture. Conv3D denotes a 3D convolutional layer; c denotes the number of channels in the layer output; k denotes the kernel (also referred to as filter) size; s denotes the size of the stride; BN denotes a batch normalization layer; ReLu denotes an rectified linear activation layer, Add denotes a addition with the identity; UnSampling denotes a UnSampling layer that expands the matrix dimension using nearest neighbor method, and Padding denotes a padding layer using the reflection padding technique. Total params: 8,337,057, trainable params: 8,331,745, non-trainable params: 5,312.

Part	Layer	Output Shape
Input		(96,200,24,3)
Encode 1	Conv3D(c16k3s2)/BN/ReLu	(48,100,12,16)
Encode 2	Conv3D(c32k3s1)/BN/ReLu	(48,100,12,32)
Encode 3	Conv3D(c64k3s2)/BN/ReLu	(24,50,6,64)
Encode 4	Conv3D(c64k3s1)/BN/ReLu	(24,50,6,64)
Encode 5	Conv3D(c128k3s2)/BN/ReLu	(12,25,3,128)
Encode 6	Conv3D(c128k3s1)/BN/ReLu	(12,25,3,128)
ResConv 1	Conv3D(c128k3s1)/BN/Conv3D(c128k3s1)/BN/ReLu/Add	(12,25,3,128)
ResConv 2	Conv3D(c128k3s1)/BN/Conv3D(c128k3s1)/BN/ReLu/Add	(12,25,3,128)
ResConv 3	Conv3D(c128k3s1)/BN/Conv3D(c128k3s1)/BN/ReLu/Add	(12,25,3,128)
ResConv 4	Conv3D(c128k3s1)/BN/Conv3D(c128k3s1)/BN/ReLu/Add	(12,25,3,128)
ResConv 5	Conv3D(c128k3s1)/BN/Conv3D(c128k3s1)/BN/ReLu/Add	(12,25,3,128)
ResConv 6	Conv3D(c128k3s1)/BN/Conv3D(c128k3s1)/BN/ReLu/Add	(12,25,3,128)
ResConv 7	Conv3D(c128k3s1)/BN/Conv3D(c128k3s1)/BN/ReLu/Add	(12,25,3,128)
Decode 6	Unpool/Padding/Conv3D(c128k3s1)/BN/Relu	(12,25,3,128)
Decode 5	Unpool/Padding/Conv3D(c128k3s2)/BN/Relu	(24,50,6,128)
Decode 4	Unpool/Padding/Conv3D(c64k3s1)/BN/Relu	(24,50,6,64)
Decode 3	Unpool/Padding/Conv3D(c64k3s2)/BN/Relu	(48,100,12,64)
Decode 2	Unpool/Padding/Conv3D(c32k3s1)/BN/Relu	(48,100,12,32)
Decode 1	Unpool/Padding/Conv3D(c16k3s2)/BN/Relu	(96,200,24,16)
Output	Conv3D(c1k3s1)	(96,200,24,1)

Appendix G. Multivariate regression

Using the data set described above, we randomly split 80% of the data into the training set and 20% into the validation set to develop the relationship between sweep efficiency, solubility trapping and a large variety of dimensionless variables. The variables include dimensionless numbers such as Bond Number ($N_b = \Delta\rho g b_{res}/P_c$ where b_{res} is reservoir thickness), Capillary number (N_c), and Gravity number (N_g), as well as dimensionless reservoir properties, including permeability (k/k_{ref}), initial pressure (P/P_{ref}), injection rate (r_{inj}/r_{ref}), perforation thickness to reservoir thickness (b_{perf}/b_{res} where b_{perf} is perforation thickness), perforation depth to reservoir thickness (l_{perf}/b_{res} where l_{perf} is perforation depth from the reservoir top), irreducible water saturation (S_{wi}), and capillary pressure curve scaling factor (λ in Equation 7). We also investigated various combinations and variations (such as reciprocals) of these aforementioned variables.

Using those relationships to inform our model, we ran a sequence of single-variable and multi-variable linear and nonlinear regressions on a training data set. We used forward variable selection with criteria of R^2 , Adjusted R^2 , and root mean squared error (RMSE) to assess the quality of the model. The Adjusted R^2 penalizes additional variables to reduce the number of variables used in the prediction. Concurrently, we used the Normal Q-Q plot to examine whether the residuals were normally distributed; the scale-location plot to monitor the constant variance assumption; the residuals versus fitted values plot to evaluate whether the data set shows non-constant variance or non-linear trends; and the Cook's distance plots to identify outliers that might significantly influence the model.

Using these diagnostic plots and the quality criterion, we discovered the optimal model for sweep efficiency with N_b , r_{inj}/r_{ref} , and S_{wi} , and for solubility trapping, a model with S_{wi} , N_b , λ , k_{ref}/k , P/P_{ref} , and T/T_{ref} . Details on the models' parameters and criterion results are summarized in Table G.7.

Table G.7: Prediction ranges, constants, quality criterion, and term standard errors for the sweep efficiency and solubility trapping estimation equations. Standard error for each term is calculated based on the the term value and the training set.

Sweep efficiency	category	parameter	value	unit
	Prediction range	N_b	10 to 450	-
		r_{inj}	0.02 to 2.0	MT/yr
		S_{wi}	0.1 to 0.3	-
	Constant	r_{ref}	1	MT/yr
		ϵ	0.01266	-
	Standard error	$\ln(N_b)$	3.56e-03	-
		N_b	4.38e-05	-
		$\ln(\frac{r_{inj}}{r_{ref}})$	2.32e-03	-
		S_{wi}	3.02e-02	-
	Quality criterion	training RMSE	0.109	-
		training R-Squared	0.964	-
		training Adjusted R-Squared	0.964	-
		validation RMSE	0.116	-
		validation R-Squared	0.962	-
		validation Adjusted R-Squared	0.962	-
Solubility trapping	category	parameter	value	unit
	Prediction range	S_{wi}	0.1 to 0.3	-
		N_b	10 to 450	-
		k	5 to 1000	mD
		λ	0.3 to 0.7	-
		P	80 to 160	bar
		T	40 to 100	C°
	Constant	k_{ref}	1	mD
		P_{ref}	250	bar
		T_{ref}	40	C°
		ϵ	6.0165e-5	-
	Standard error	$\ln(N_b)$	2.10e-04	-
		$\frac{k_{ref}}{k}$	3.94e-03	-
		λ	1.28e-03	-
		S_{wi}	2.42e-03	-
		$\frac{T}{T_{ref}}$	6.30e-04	-
		$\frac{P}{P_{ref}}$	2.27e-03	-
	Quality criterion	training RMSE	0.008	-
		training R-Squared	0.845	-
		training Adjusted R-Squared	0.845	-
		validation RMSE	0.008	-
		validation R-Squared	0.833	-
		validation Adjusted R-Squared	0.834	-

References

- [1] K. Aziz, Petroleum reservoir simulation, Applied Science Publishers 476 (1979).
- [2] R. K. Pachauri, M. R. Allen, V. R. Barros, J. Broome, W. Cramer, R. Christ, J. A. Church, L. Clarke, Q. Dahe, P. Dasgupta, et al., Climate change 2014: synthesis report. Contribution of Working Groups I, II and III to the fifth assessment report of the Intergovernmental Panel on Climate Change, Ipcc, 2014.
- [3] M. B. Allen III, Numerical modelling of multiphase flow in porous media, *Advances in Water Resources* 8 (4) (1985) 162–187.
- [4] G. L. Chierici, The simulation of reservoir behaviour using numerical modelling, in: *Principles of Petroleum Reservoir Engineering*, Springer, 1995, pp. 123–229.
- [5] K. Pruess, ECO2N: A TOUGH2 fluid property module for mixtures of water, NaCl, and CO₂, Lawrence Berkeley National Laboratory Berkeley, CA, 2005.
- [6] O. Khebzegga, A. Iranshahr, H. Tchelepi, Continuous relative permeability model for compositional simulation, *Transport in Porous Media* 134 (1) (2020) 139–172.
- [7] F. M. Orr, et al., *Theory of gas injection processes*, Vol. 5, Tie-Line Publications Copenhagen, 2007.
- [8] R. Pini, S. C. Krevor, S. M. Benson, Capillary pressure and heterogeneity for the CO₂/water system in sandstone rocks at reservoir conditions, *Advances in Water Resources* 38 (2012) 48–59.
- [9] C. Doughty, Investigation of CO₂ plume behavior for a large-scale pilot test of geologic carbon storage in a saline formation, *Transport in porous media* 82 (1) (2010) 49–76.
- [10] G. Wen, S. M. Benson, CO₂ plume migration and dissolution in layered reservoirs, *International Journal of Greenhouse Gas Control* 87 (May) (2019) 66–79. doi:10.1016/j.ijggc.2019.05.012.
URL <https://linkinghub.elsevier.com/retrieve/pii/S1750583619300246>

- [11] P. K. Kitanidis, Persistent questions of heterogeneity, uncertainty, and scale in subsurface flow and transport, *Water Resources Research* 51 (8) (2015) 5888–5904. doi:10.1002/2015WR017639.
- [12] M. A. Cardoso, L. J. Durlofsky, P. Sarma, Development and application of reduced-order modeling procedures for subsurface flow simulation, *International journal for numerical methods in engineering* 77 (9) (2009) 1322–1350.
- [13] S. Razavi, B. A. Tolson, D. H. Burn, Review of surrogate modeling in water resources, *Water Resources Research* 48 (7) (2012).
- [14] H. Bazargan, M. Christie, A. H. Elsheikh, M. Ahmadi, Surrogate accelerated sampling of reservoir models with complex structures using sparse polynomial chaos expansion, *Advances in Water Resources* 86 (2015) 385–399.
- [15] H. Hamdi, I. Couckuyt, M. C. Sousa, T. Dhaene, Gaussian processes for history-matching: application to an unconventional gas reservoir, *Computational Geosciences* 21 (2) (2017) 267–287.
- [16] L. Tian, R. Wilkinson, Z. Yang, H. Power, F. Fagerlund, A. Niemi, Gaussian process emulators for quantifying uncertainty in co2 spreading predictions in heterogeneous media, *Computers & Geosciences* 105 (2017) 113–119.
- [17] M. Tang, Y. Liu, L. J. Durlofsky, A deep-learning-based surrogate model for data assimilation in dynamic subsurface flow problems, *Journal of Computational Physics* 413 (2020) 109456.
- [18] Z. L. Jin, Y. Liu, L. J. Durlofsky, Deep-learning-based surrogate model for reservoir simulation with time-varying well controls, *Journal of Petroleum Science and Engineering* 192 (2020) 107273.
- [19] S. Mo, Y. Zhu, N. Zabararas, X. Shi, J. Wu, Deep convolutional encoder-decoder networks for uncertainty quantification of dynamic multiphase flow in heterogeneous media, *Water Resources Research* 55 (1) (2019) 703–728.
- [20] Z. Zhong, A. Y. Sun, B. Ren, Y. Wang, A deep-learning-based approach for reservoir production forecast under uncertainty, *SPE Journal* 1 1–27.

- [21] P. IEA, Ccus in clean energy transitions, Tech. rep. (2020).
URL <https://www.iea.org/reports/ccus-in-clean-energy-transitions>
- [22] H. Yamamoto, C. Doughty, Investigation of gridding effects for numerical simulations of co2 geologic sequestration, *International Journal of Greenhouse Gas Control* 5 (4) (2011) 975–985.
- [23] H. Yamamoto, C. Doughty, Investigation of gridding effects for numerical simulations of CO2 geologic sequestration, *International Journal of Greenhouse Gas Control* 5 (4) (2011) 975–985. doi:10.1016/j.ijggc.2011.02.007.
URL <http://dx.doi.org/10.1016/j.ijggc.2011.02.007>
- [24] E. Saadatpoor, S. L. Bryant, K. Sepehrnoori, New trapping mechanism in carbon sequestration, *Transport in Porous Media* 82 (1) (2010) 3–17. doi:10.1007/s11242-009-9446-6.
- [25] S. Krevor, M. J. Blunt, S. M. Benson, C. H. Pentland, C. Reynolds, A. Al-Menhali, B. Niu, Capillary trapping for geologic carbon dioxide storage - From pore scale physics to field scale implications, *International Journal of Greenhouse Gas Control* 40 (2015) 221–237. doi:10.1016/j.ijggc.2015.04.006.
URL <http://dx.doi.org/10.1016/j.ijggc.2015.04.006>
- [26] S. T. Ide, K. Jessen, F. M. Orr, Storage of CO2 in saline aquifers: Effects of gravity, viscous, and capillary forces on amount and timing of trapping, *International Journal of Greenhouse Gas Control* 1 (4) (2007) 481–491. doi:10.1016/S1750-5836(07)00091-6.
- [27] K. Pruess, J. Nordbotten, Numerical simulation studies of the long-term evolution of a co 2 plume in a saline aquifer with a sloping caprock, *Transport in porous media* 90 (1) (2011) 135–151.
- [28] Y. Zhu, N. Zabaras, P. S. Koutsourelakis, P. Perdikaris, Physics-constrained deep learning for high-dimensional surrogate modeling and uncertainty quantification without labeled data, *Journal of Computational Physics* 394 (2019) 56–81. arXiv:1901.06314, doi:10.1016/j.jcp.2019.05.024.
URL <https://doi.org/10.1016/j.jcp.2019.05.024>

- [29] O. Fuks, H. Tchelepi, Physics based deep learning for nonlinear two-phase flow in porous media, in: ECMOR XVII, Vol. 2020, European Association of Geoscientists & Engineers, 2020, pp. 1–10.
- [30] G. Wen, M. Tang, S. M. Benson, Towards a predictor for co2 plume migration using deep neural networks, International Journal of Greenhouse Gas Control 105 (2021) 103223. doi:<https://doi.org/10.1016/j.ijggc.2020.103223>. URL <http://www.sciencedirect.com/science/article/pii/S1750583620306484>
- [31] H. Wu, R. Qiao, Physics-constrained deep learning for data assimilation of subsurface transport, Energy and AI 3 (2020) 100044.
- [32] Q. He, D. Barajas-Solano, G. Tartakovsky, A. M. Tartakovsky, Physics-informed neural networks for multiphysics data assimilation with application to subsurface transport, Advances in Water Resources 141 (2020) 103610.
- [33] M. Liu, D. Grana, Petrophysical characterization of deep saline aquifers for co2 storage using ensemble smoother and deep convolutional autoencoder, Advances in Water Resources 142 (2020) 103634.
- [34] Z. Jiang, P. Tahmasebi, Z. Mao, Deep residual u-net convolution neural networks with autoregressive strategy for fluid flow predictions in large-scale geosystems, Advances in Water Resources (2021) 103878.
- [35] E. Haghghat, R. Juanes, Sciann: A keras/tensorflow wrapper for scientific computations and physics-informed deep learning using artificial neural networks, Computer Methods in Applied Mechanics and Engineering 373 (2021) 113552.
- [36] Z. Zhong, A. Y. Sun, H. Jeong, Predicting co2 plume migration in heterogeneous formations using conditional deep convolutional generative adversarial network, Water Resources Research 55 (7) (2019) 5830–5851.
- [37] S. Haykin, Neural Networks and Learning Machines, 3/E, Pearson Education India, 2010.

- [38] K. Pruess, C. M. Oldenburg, G. Moridis, Tough2 user’s guide version 2, Tech. rep., Lawrence Berkeley National Lab.(LBNL), Berkeley, CA (United States) (1999).
- [39] Schlumberger, Eclipse reservoir simulation software reference manual (2014).
- [40] Global CCS Institute, Ccs facilities database co2re, data retrieved from: <https://co2re.co/> (2020).
- [41] NAS, Negative Emissions Technologies and Reliable Sequestration, 2018. doi:10.17226/25259.
- [42] S. C. Krevor, R. Pini, L. Zuo, S. M. Benson, Relative permeability and trapping of co2 and water in sandstone rocks at reservoir conditions, *Water resources research* 48 (2) (2012).
- [43] S. Benson, R. Pini, C. Reynolds, S. Krevor, Relative permeability analyses to describe multi-phase flow in co2 storage reservoirs, Global CCS Institute (2013).
- [44] D. Tran, L. Bourdev, R. Fergus, L. Torresani, M. Paluri, Learning spatiotemporal features with 3d convolutional networks, in: *Proceedings of the IEEE international conference on computer vision*, 2015, pp. 4489–4497.
- [45] S. Song, C. Lan, J. Xing, W. Zeng, J. Liu, An end-to-end spatio-temporal attention model for human action recognition from skeleton data, in: *Proceedings of the AAAI conference on artificial intelligence*, Vol. 31, 2017.
- [46] S. Xie, C. Sun, J. Huang, Z. Tu, K. Murphy, Rethinking spatiotemporal feature learning: Speed-accuracy trade-offs in video classification, in: *Proceedings of the European Conference on Computer Vision (ECCV)*, 2018, pp. 305–321.
- [47] K. He, X. Zhang, S. Ren, J. Sun, Deep residual learning for image recognition, in: *Proceedings of the IEEE conference on computer vision and pattern recognition*, 2016, pp. 770–778.

- [48] O. Ronneberger, P. Fischer, T. Brox, U-net: Convolutional networks for biomedical image segmentation, in: International Conference on Medical image computing and computer-assisted intervention, Springer, 2015, pp. 234–241.
- [49] D. P. Kingma, J. Ba, Adam: A method for stochastic optimization, arXiv preprint arXiv:1412.6980 1 (2014).
- [50] X. Glorot, Y. Bengio, Understanding the difficulty of training deep feed-forward neural networks, in: Proceedings of the thirteenth international conference on artificial intelligence and statistics, JMLR Workshop and Conference Proceedings, 2010, pp. 249–256.
- [51] L. Van der Meer, The co2 storage efficiency of aquifers, *Energy conversion and management* 36 (6-9) (1995) 513–518.
- [52] R. Okwen, S. Frailey, H. Leetaru, S. Moulton, Assessing reservoir depositional environments to develop and quantify improvements in co2 storage efficiency. a reservoir simulation approach, Tech. rep., University of Illinois, Champaign, IL (United States) (2014).
- [53] W. D. Gunter, S. Bachu, S. Benson, The role of hydrogeological and geochemical trapping in sedimentary basins for secure geological storage of carbon dioxide, Geological Society, London, Special Publications 233 (1) (2004) 129–145.
- [54] S. M. Gilfillan, B. S. Lollar, G. Holland, D. Blagburn, S. Stevens, M. Schoell, M. Cassidy, Z. Ding, Z. Zhou, G. Lacrampe-Couloume, et al., Solubility trapping in formation water as dominant co 2 sink in natural gas fields, *Nature* 458 (7238) (2009) 614–618.
- [55] T. Suekane, T. Nobuso, S. Hirai, M. Kiyota, Geological storage of carbon dioxide by residual gas and solubility trapping, *International Journal of Greenhouse Gas Control* 2 (1) (2008) 58–64.
- [56] A. Riaz, M. Hesse, H. Tchelepi, F. Orr, Onset of convection in a gravitationally unstable diffusive boundary layer in porous media, *Journal of Fluid Mechanics* 548 (1) (2006) 87–111.

- [57] C. W. MacMinn, J. A. Neufeld, M. A. Hesse, H. E. Huppert, Spreading and convective dissolution of carbon dioxide in vertically confined, horizontal aquifers, *Water Resources Research* 48 (11) (2012).
- [58] R. M. Enick, S. M. Klara, Co2 solubility in water and brine under reservoir conditions, *Chemical Engineering Communications* 90 (1) (1990) 23–33.
- [59] C. Doughty, Modeling geologic storage of carbon dioxide: comparison of non-hysteretic and hysteretic characteristic curves, *Energy Conversion and Management* 48 (6) (2007) 1768–1781.
- [60] S. Krevor, M. J. Blunt, S. M. Benson, C. H. Pentland, C. Reynolds, A. Al-Menhali, B. Niu, Capillary trapping for geologic carbon dioxide storage—from pore scale physics to field scale implications, *International Journal of Greenhouse Gas Control* 40 (2015) 221–237.
- [61] S. Bachu, W. Gunter, E. Perkins, Aquifer disposal of co2: hydrodynamic and mineral trapping, *Energy conversion and management* 35 (4) (1994) 269–279.
- [62] T. Xu, J. A. Apps, K. Pruess, Numerical simulation of co2 disposal by mineral trapping in deep aquifers, *Applied geochemistry* 19 (6) (2004) 917–936.
- [63] U. DOE, Carbon storage atlas—fifth edition (atlas v).[online]. national energy technical laboratory (2015).
- [64] U. G. S. G. C. D. S. R. A. Team, National assessment of geologic carbon dioxide storage resources—data (ver. 1.1, september 2013): U.s. geological survey data series 774, 13 p., plus 2 appendixes and 2 large tables in separate files (2013).
URL <https://pubs.usgs.gov/ds/774/>
- [65] B. of Ocean Energy Management, Atlas of gulf of mexico gas and oil sands data.
URL <https://www.data.boem.gov/Main/GandG.aspx>
- [66] N. Remy, A. Boucher, J. Wu, Applied Geostatistics with SGeMS: A User’s Guide, Cambridge University Press, 2009. doi:10.1017/CB09781139150019.

- [67] S. Carpentier, K. Roy-Chowdhury, Conservation of lateral stochastic structure of a medium in its simulated seismic response, *Journal of Geophysical Research: Solid Earth* 114 (B10) (2009).